Structures 70 (2024) 107573

Contents lists available at ScienceDirect

Structures

journal homepage: www.elsevier.com/locate/structures

Structural behaviour and design of wire arc additively manufactured bolted connections with thick plates

Yunyi Liu [a], Jun Ye [b,*], Hongjia Lu [c], Guan Quan [a], Zhen Wang [d], Yang Zhao [e], Weijian Zhao [a]

[a] College of Civil Engineering and Architecture, Zhejiang University, Hangzhou 310058, China
[b] School of Civil Engineering, University of Leeds, Leeds LS2 9JT, UK
[c] Centre for Innovative Structures and Materials, School of Engineering, RMIT University, Melbourne 3001, Australia
[d] Department of Civil Engineering, Hangzhou City University, Hangzhou 310015, China
[e] School of Civil Engineering, Shaoxing University, Shaoxing, China

ARTICLE INFO

Keywords:
Metal 3D printing
Wire arc additive manufacturing
Single-shear bolt connections
Failure modes
Design approaches

ABSTRACT

The application of additive manufacturing technology in the construction industry is currently a popular topic around the world. However, the research on the structural behaviour of thick plates produced via Wire and Arc Additive Manufacturing (WAAM) technology has been limited, despite the demand for such components in large-scale constructions that is subjected to large actions. This paper investigated the structural behaviour and design of WAAM single-shear bolted connections with thick plates with failure modes of net section, tilt-bearing, and end-splitting failure. The mechanical properties of the material were first determined by means of tensile coupon tests. An experimental programme of 32 sets of bolted connections with varying dimensions and print layer orientations was conducted. An anisotropic behaviour of WAAM steel bolted connections with different print layer orientations was observed, which had an influence on their failure modes and ultimate capacities. The experimental results were analysed and compared to the predictions using existing design approaches corresponding to conventional steel bolted connections. The comparison showed that these approaches were applicable to WAAM steel bolted connections, but there were still some limitations in the existing design guidelines. This research can contribute to the application of 3D printing technology in constructions.

1. Introduction

Over the past decade, additive manufacturing (AM) has undergone significant evolution, transitioning from its origins in rapid prototyping to encompass mass production and the construction of large-scale structures. Among various AM techniques, Wire and Arc Additive Manufacturing technology (WAAM) is a process that creates components through the successive layer-by-layer deposition of material, as shown in Fig. 1. It stands out as a cutting-edge method in the metal AM sector, surpassing other methods such as powder bed laser fusion and electron beam melting in terms of printing speed, cost efficiency, sustainability, and the ability for large-scale production [1–4].

This unique set of attributes makes WAAM exceptionally well-suited for application in the Civil Engineering construction field. Its efficacy has been prominently displayed in the manufacturing of the WAAM steel bolted connection [5], cantilever truss [6], and footbridges [7,8], demonstrating its potential as an innovative method in construction, as shown in Fig. 2.

To effectively integrate the design of metal components produced through WAAM into existing design codes, a comprehensive understanding of their mechanical and structural characteristics is essential. Associated research has highlighted the notable anisotropy of WAAM steels dependent on print layer orientations [9–15]. These studies emphasize the need for new constitutive models tailored to WAAM steels, facilitating numerical simulations and further practical application [16]. Furthermore, investigations into the structural performance and fatigue behaviour of WAAM-fabricated elements, including walls, beams, columns, and joints, have been undertaken [5,17–27]. Additionally, several studies have combined WAAM technology with topology optimization, utilizing the high degree of geometric freedom of WAAM technology to fabricate optimized beams, trusses, and joints with high material utilization [5,6,28,29]. Due to manufacturing constraints, large-scale and complex metallic structures produced via WAAM technology need to be printed in sections and assembled using bolted

* Corresponding author.
E-mail address: J.Ye2@leeds.ac.uk (J. Ye).

https://doi.org/10.1016/j.istruc.2024.107573
Received 10 July 2024; Received in revised form 7 October 2024; Accepted 11 October 2024
Available online 24 October 2024

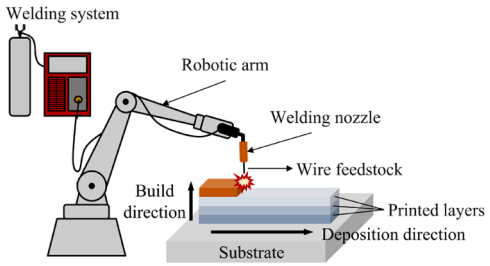

Fig. 1. Manufacturing equipment and printed specimens of WAAM process.

connections. This has led to growing interest in the study of WAAM steel bolted connections, as ensuring their integration into traditional prefabricated structural systems remains a critical area of research.

Previously, the structural behaviours of conventionally manufactured steel bolted connections have been well investigated. These explorations have identified various failure modes in the connected plates from bolted connection tests, including net section tension, shear-out, end-splitting, bearing, and tilt-bearing, as shown in Fig. 3. Some new design equations have also been developed for the analysis of connections with these failure modes [30–36]. The behaviour of these bolted connections is predominantly determined by their geometric dimensions [37–41], including plate width, end distances, and plate thicknesses. Subsequently, with the increased use of thick steel plates in building and bridge construction, the examination of connections between these thick plates is also important [42]. In the WAAM process, thick plates are constructed by different printing strategies and parameters, leading to potential variance in material properties when compared to thin plates. Guo et al. [30,31] tested the structural behaviours of WAAM steel bolted connections with both thin (3 mm) and thick (8 mm) plates, and compared the results to the standards set for cold-formed steel. However, the differences between the two thickness categories may need more detailed discussions. At present, there is a lack of design provisions tailored for WAAM steel bolted connections. Current design methods borrowed from conventional design codes, such as AS 4100 [43], AISC 360 [44], and Eurocode equations [45,46] for WAAM connections may lead to the inferior predictions of capacities and failure modes. To promote the development of design provisions for WAAM steel bolted connections, comprehensive bolted connection tests and analytical comparisons with existing design guidelines are required.

Therefore, this study conducted tensile coupon tests on 19 specimens and single-shear bolted connection tests on 32 specimens made from 8 mm thick carbon steel plates using WAAM technology. The geometries of the specimens were measured using a 3D laser scanner and tested using digital image correlation (DIC) to measure the experimental response. The test results were analysed in terms of material anisotropic behaviour and were compared with the predictions of current design provisions. Additionally, the experimental responses and adaptability to design provisions of WAAM steel bolted connections were compared to previous research of thin plated connections. This study provides an in-depth analysis of the material properties and structural behaviour of WAAM thick bolted connections, promoting the implementation of 3D printing technology in construction.

2. Available design provisions

Although design equations for 3D-printed bolted connections with thick plates have not yet been developed, existing methods for conventionally manufactured steel can be adapted to account for the unique material behaviour of WAAM steel. To evaluate the design suitability of WAAM steel bolted connections, particularly for plates thicker than 8 mm, relevant design provisions for various failure modes were reviewed.

2.1. AS 4100 [43]

The AS 4100 [43] was developed by Standards Australia Committee for steel structures. For bolted connection specimens depicted in Fig. 4, the ultimate capacity of the net section tension failure mode can be calculated using Eq. (1a). Whilst for shear out failure and bearing failure modes, the ultimate capacities are calculated using Eqs. (1b) and (1c). The final capacity for a given connection is determined by the lowest calculated value among these, with the failure mode being the one corresponding to this minimum value.

$$P_{ns,AS} = 0.85 A_n f_u \tag{1a}$$

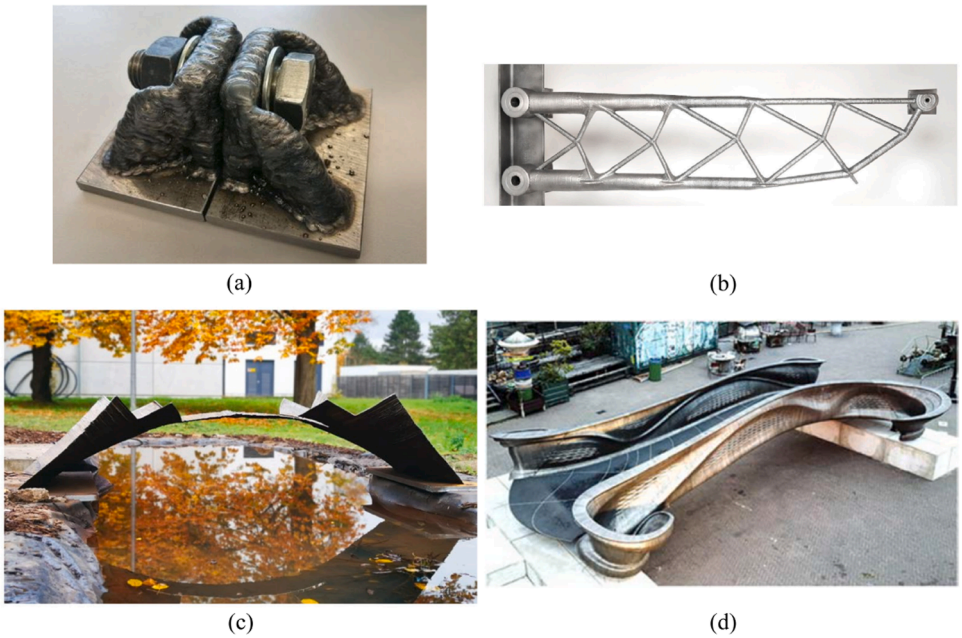

Fig. 2. WAAM steel structures: (a) a bolted connection [5], (b) a cantilever truss [6], (c) a small 3D printed footbridge in shell form [7], and (d) a MX3D metal 3D printed footbridge [8].

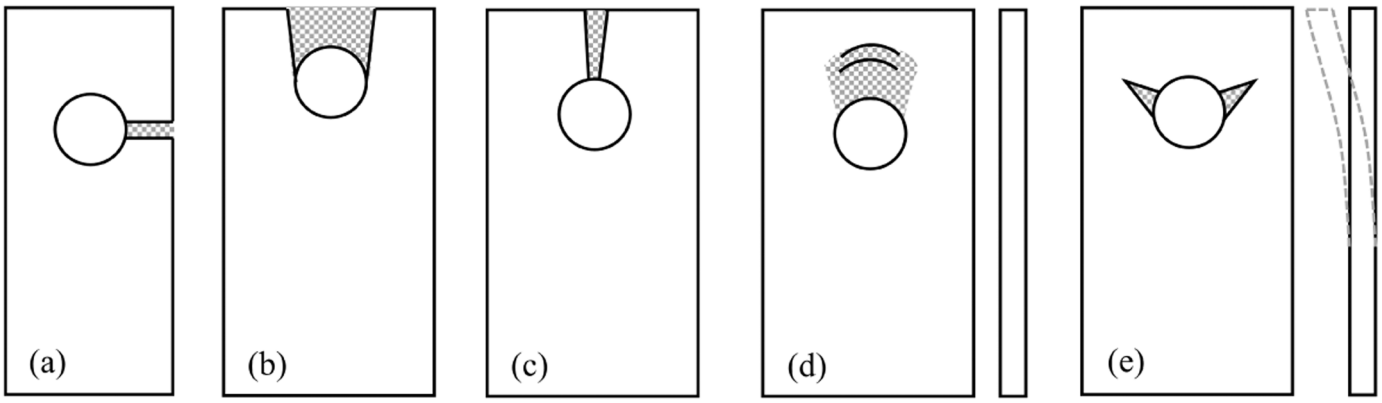

Fig. 3. Schematic diagrams of various failure modes: (a) net section tension, (b) shear-out, (c) end-splitting, (d) bearing, and (e) tilt-bearing failure.

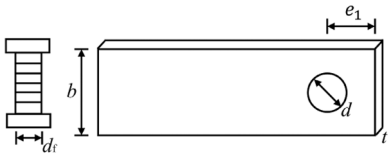

Fig. 4. The geometric characteristics of a bolted connection specimen.

$$P_{so,AS} = (e_1 - \frac{d}{2})tf_u \quad (1b)$$

$$P_{b,AS} = 3.2d_f tf_u \quad (1c)$$

where, A_n is a net sectional area of the connection plate; f_u denotes the tensile strength of the connection plate; e_1 is the distance between the centre of a standard bolt hole to the end of the connection plate; t is the thickness of the connection plates; d is the nominal bolt hole diameter; and d_f is the nominal bolt diameter.

2.2. AISC 360 [44]

The AISC 360:2020 [44] was developed by American National Standards Institute for structural steel buildings. Similar to AS 4100 code [43], the nominal capacity of a connection is determined by the lowest calculated capacity among the net section tension, shear out, and bearing failure modes. The final predicted failure mode corresponds to the failure mode associated with the lowest value, as detailed in Eqs. (2a), (2b) and (2c), respectively.

$$P_{ns,AISC} = A_n f_u \quad (2a)$$

$$P_{so,AISC} = 1.5(e_1 - \frac{d}{2})tf_u \quad (2b)$$

$$P_{b,AISC} = 3d_f tf_u \quad (2c)$$

2.3. Eurocode 3 [45,46]

The Eurocode 3 [45,46], developed by European Committee for Standardization, covers design guidelines for steel structures. The ultimate capacities of net section tension failure modes can be calculated utilizing Eq. (3a) from EN 1993–1-1:2020 [45]. For bearing failure mode, the ultimate capacity is calculated using Eq. (3b) proposed by EN 1993–1-8:2021 [46]. The final capacity for a specific connection was determined as the lowest value, while the final predicted failure mode was the corresponding failure mode of this lowest value.

$$P_{ns,EN1} = kA_n f_u \quad (3a)$$

$$P_{EN8} = \alpha_b k_m d_f tf_u \quad (3b)$$

where $k = 1$ for plates with smooth holes fabricated by drilling or water jet cutting; or $k = 0.9$ for plates with rough holes fabricated by punching or flame cutting; α_b is the minimum of e_1/d, $3f_{ub}/f_u$, and 3; for steel grades equal to or higher than S460, $k_m = 0.9$; otherwise $k_m = 1$.

2.4. Design equations proposed in the literature

For shear out failure mode, the design equations in various codes of practices utilized different shear failure plane. AS/NZS 4600 [47] adopted the gross shear length ($L_{gv} = e_1$) whilst AS 4100 [43] used the net shear length ($L_{nv} = e_1$-$d/2$). Teh and Uz [33] proposed Eq. (4) by defining an active shear length ($L_{av} = e_1$-$d/4$) based on their experimental analysis and finite element research.

$$P_{so} = 1.2(e_1 - \frac{d}{4})tf_u \quad (4)$$

A modified Eq. (5) was proposed by Xing et al. [34] considering the catenary action which has a significant effect on the shear-out capacity.

$$P_{so} = 1.2(\frac{3d_f}{e_1})^p(e_1 - \frac{d}{4})tf_u \quad (5)$$

where p represents the degree of influence cause by catenary action. $p = 1/10$ is adopted herein for the single-shear single-bolt connections.

Based on experimental results and data analysis conducted by Teh and Uz [36], Eq. (6) was proposed for determining the ultimate tilt-bearing capacity, which was distinguished from the conventional bearing failure. It was found that variations in bolt hole clearances, material ductility, and bolt head orientation do not have noticeable effects on the ultimate tilt-bearing capacity of single-shear bolted connections.

$$P_{tb} = 2.65(b - d)d_f^{\frac{1}{2}}t^{\frac{4}{3}}f_u \quad (6)$$

3. Experimental programme

3.1. Materials and specimens

Two types of steel plates were used in the experimental programme, each pair of connections included a bolt, a WAAM steel plate and a high-strength Q690 steel plate. The tested WAAM steel plates with a nominal thickness of 8 mm were cut from oval tubes with flat sides, which were manufactured using WAAM technology following the printing parameters listed in Table 1. The used feedstock material was ER50–6 low-carbon steel, with its chemical compositions and mechanical properties listed in Table 2 and Table 3, respectively, as provided by the manufacturer. The tested high-strength Q690 steel plates with a nominal

Table 1
Printing and environmental parameters of specimens with a nominal thickness of 8 mm.

Travel speed (m/min)	Wire feed rate (m/min)	Wire diameter (mm)	Welding voltage (V)	Layer thickness (mm)	Bead width (mm)	Temperature (°C)	Humidity (%RH)	Shielding gas
0.55–0.6	6.5	1.2	23	2.7	7.5	12–21	35–55	97 %Ar+ 3 % CO_2

Table 2
Chemical compositions (% by weight) of ER50–6 low carbon steel feedstock.

Chemical compositions	C	Mn	Si	P	S	Cr	Ni	Cu	Mo	V
ER50–6	0.074	1.47	0.85	0.015	0.01	0.023	0.009	0.1	0.004	0.002

Table 3
Mechanical properties of ER50–6 low carbon steel feedstock.

	Tensile Strength (MPa)	Yield Strength (MPa)	Elongation Rate (%)	Charpy V Impact Test Value at 40 ℃ (J)
ER50–6	554	445	26	96

thickness of 8 mm were used to replace parts of WAAM steel plates in the bolted connections, to simplify the experimental variables and to ensure the failure occurring on the WAAM steel plates.

A total of 32 WAAM steel bolted connection specimens were tested to investigate the influences of geometric parameters, including the diameter of the bolt hole d, the width of the connected plate b, the minimum distance from the centre of the bolt hole to the end of the connected plate e_1 (end distance), and the thickness of the connected plate t (as illustrated in Fig. 5). $e_1 \in [1.4d, \quad 2.5d]$ and $e_2 \in [0.9d, \quad 1.8d]$ were utilized in this study, with e_2 denoting half of the width b. The different geometry combinations of e_1/d and e_2/d of connected plates resulted in different experimental responses. For 16 configurations of geometry, two specimens with θ of 0° and 90° are manufactured respectively, where θ represents the angle between the specimen axis and the print layer orientations, as shown in Fig. 5. This approach was employed to investigate the potential effects of print layer orientations on the experimental response of the WAAM steel bolted connection specimens.

Each WAAM single-shear connected plate is named in the form of HS8-*d*-*b*- e_1 or VS8-*d*-*b*- e_1 with nominal dimensions. 'H' or 'V' represent that the plate was extracted horizontally or vertically to the print layer orientation, with θ being 0° or 90°, respectively. 'S' denotes the single-shear connection type, followed by the nominal thickness t of 8 mm. The high-strength steel plates are named following the same form of WAAM plates, such as HSS8–26-50–39, with "HSS" denoting high-strength steel.

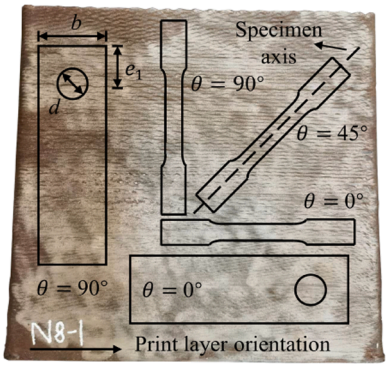

Fig. 5. The basic configuration of tested specimens extracted from flat plates at different orientations.

3.2. Geometric measurements

Due to the undulating surfaces of the WAAM steel plates, a 3D laser scanner, SIMSCAN from SCANTECH, was used to measure the physical geometric dimensions of the WAAM plates and high-strength plates. The scanning process is depicted in Fig. 6, with more detailed information provided in previous studies [48,49]. The obtained geometric measurement results of WAAM steel plates and high-strength steel plates are shown in Table 4.

3.3. Test arrangements

All tested specimens were single-shear single-bolted connections, and each specimen was composed of a WAAM plate and a matched high-strength steel plate, connected using a finger-tightened bolt in a 2 mm clearance hole, as shown in Fig. 7. The grade 12.9 fully threaded bolts with nominal diameters of 24 mm and 30 mm were used to prevent bolt shearing, ensuring that the fracture occurred in the WAAM plates. Auxiliary plates were added at the clamping end to load the bolted connection specimens under concentric load.

A DIC system was utilised to conduct a non-contact full-field measurement, with a camera monitoring the displacements of the unfixed plates at a frequency of 5 Hz. All specimens were painted white and black in turn to form random speckle patterns for DIC tracking displacements. An extensometer with a gauge length of 150 mm was also set up to verify the displacements measured by the DIC system, which extracted a length of 150 mm at the same location to calculate the matched displacements. The results obtained from the DIC system and the extensometer showed a negligible difference of less than 6 %. As a result, data from the DIC system was used for subsequent data analysis.

The coupon specimens and bolted connection specimens were tested to failure using a 250 kN Instron 8802 testing machine under displacement control mode at a stroke rate of 0.8 mm/min and 1.0 mm/min, respectively. The test setup is shown in Fig. 7. Individual specimens with high ultimate capacities were tested to failure using a 1000 kN Instron 8805 testing machine.

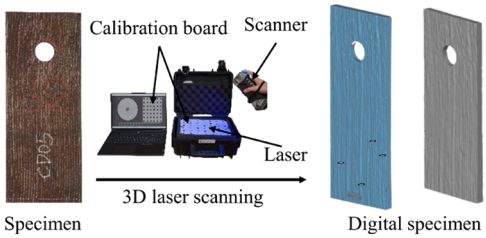

Fig. 6. The scanning process.

Table 4
Geometric measurement results of WAAM steel plates and high-strength steel plates.

Specimens	d_f (mm)	t (mm)	d (mm)	b (mm)	e_1 (mm)	Matched specimens	t_{HSS} (mm)	d_{HSS} (mm)	b_{HSS} (mm)	$e_{1,HSS}$ (mm)
HS8-26-50-39	24.0	8.3	26.2	49.0	38.1	HSS-26-50-39	7.86	26.7	50.2	40.3
HS8-26-60-39	24.0	8.4	26.2	59.2	39.5	HSS-26-60-39	7.94	25.8	60.2	39.5
HS8-26-70-39	24.0	8.9	26.0	70.4	37.8	HSS-26-70-39	7.94	26.4	70.1	40.4
HS8-26-90-39	24.0	8.3	26.2	90.3	37.9	HSS-26-90-39	7.96	26.6	90.7	39.3
HS8-26-90-44	24.0	8.3	25.6	90.5	42.4	HSS-26-90-44	7.85	26.2	90.6	43.8
HS8-26-60-50	24.0	8.4	26.0	59.1	49.6	HSS-26-60-50	7.87	26.4	60.4	50.6
HS8-26-90-52	24.0	8.1	26.4	90.0	51.6	HSS-26-90-52	7.98	26.6	91.0	52.9
HS8-26-90-57	24.0	8.3	25.8	90.3	56.7	HSS-26-90-57	7.97	26.7	90.6	57.0
HS8-26-90-65	24.0	8.4	26.2	90.3	64.9	HSS-26-90-65	7.97	26.7	90.7	64.8
HS8-32-60-48	30.0	8.8	32.4	59.7	47.2	HSS-32-60-48	7.94	31.9	60.8	48.7
HS8-32-70-48	30.0	8.5	32.8	70.3	47.4	HSS-32-70-48	7.92	32.4	70.6	48.4
HS8-32-90-48	30.0	8.4	32.2	90.4	47.3	HSS-32-90-48	7.96	32.1	91.4	47.3
HS8-32-90-42	30.0	9.0	32.4	91.2	39.8	HSS-32-90-42	7.97	32.0	90.7	41.4
HS8-32-90-64	30.0	9.0	32.6	91.3	63.5	HSS-32-90-64	7.95	32.1	91.0	62.9
HS8-32-70-45	30.0	9.0	32.8	71.4	44.7	HSS-32-70-45	7.98	32.0	71.5	44.8
HS8-32-100-58	30.0	8.6	32.4	99.2	58.2	HSS-32-100-58	7.96	32.5	100.2	57.8
HS8-32-100-64	30.0	8.3	32.4	99.9	63.4	HSS-32-100-64	7.95	32.3	100.4	63.6
VS8-26-50-39	24.0	8.7	26.0	48.8	39.0	VSS-26-50-39	7.99	26.6	50.5	39.2
VS8-26-60-39	24.0	9.3	26.2	60.5	38.3	VSS-26-60-39	7.94	26.6	60.9	39.9
VS8-26-70-39	24.0	8.3	26.0	70.1	36.4	VSS-26-70-39	7.88	26.7	70.1	39.1
VS8-26-90-39	24.0	9.4	25.6	89.9	38.6	VSS-26-90-39	7.92	26.6	90.4	39.4
VS8-26-90-44	24.0	8.4	26.0	89.9	44.2	VSS-26-90-44	7.91	26.5	90.7	43.8
VS8-26-60-50	24.0	8.4	26.0	60.4	51.4	VSS-26-60-50	7.94	26.6	60.8	50.4
VS8-26-90-32	24.0	9.7	25.8	89.8	31.7	VSS-26-90-32	7.96	26.6	90.2	32.4
VS8-26-90-52	24.0	8.6	26.0	89.8	52.2	VSS-26-90-52	8.01	26.6	90.1	52.0
VS8-26-90-57	24.0	9.5	26.0	90.1	56.0	VSS-26-90-57	7.86	26.7	91.1	57.5
VS8-26-90-65	24.0	8.8	26.2	90.3	64.1	VSS-26-90-65	7.96	26.6	90.2	65.4
VS8-32-90-48	30.0	9.5	33.2	90.0	48.4	VSS-32-90-48	7.87	32.7	90.3	48.4
VS8-32-90-64	30.0	8.6	32.2	90.2	62.9	VSS-32-90-64	7.95	32.3	90.6	64.3
VS8-32-90-39	30.0	9.2	32.8	90.4	38.2	VSS-32-90-39	7.97	32.3	89.9	38.5
VS8-32-100-58	30.0	9.0	32.2	98.7	58.1	VSS-32-100-58	8.01	32.4	100.9	57.1
VS8-32-100-64	30.0	8.9	31.8	100.2	63.1	VSS-32-100-64	7.99	31.5	100.6	63.4

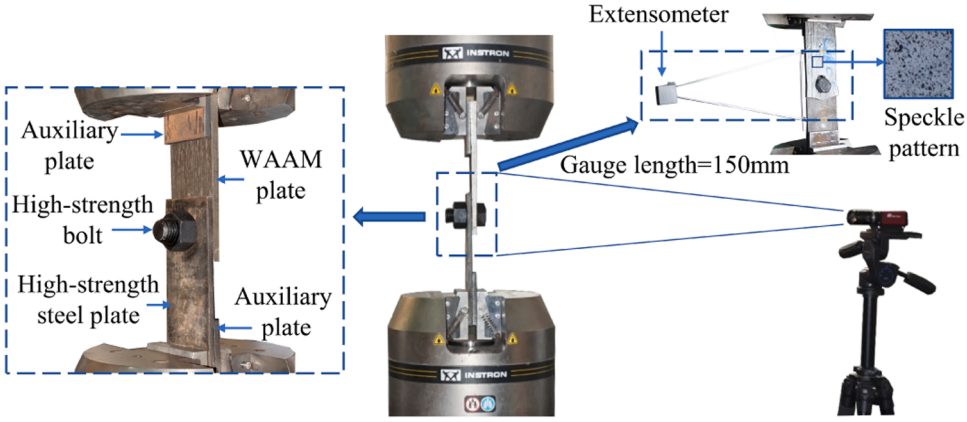

Fig. 7. The test setup.

4. Test results

4.1. Tensile coupon tests

4.1.1. Geometric properties

The process of scanning and geometric measurement of the specimens were shown in Fig. 8. The geometric measurements were executed on a series of cross-section profiles extracted from the parallel segments of coupons. The average geometric properties are shown in Fig. 9, where t, e_y, and e_z represent the average of thickness and eccentricity between the centroid of coupon and cross-section along the Y-axis and Z-axis shown in Fig. 8; t_{std}, $e_{y,std}$, $e_{z,std}$ represent the standard deviation values of thickness and eccentricity between the centroid of coupon and cross-section along the Y-axis and Z-axis.

The eccentricities e_z were generally slightly higher than e_y, indicating

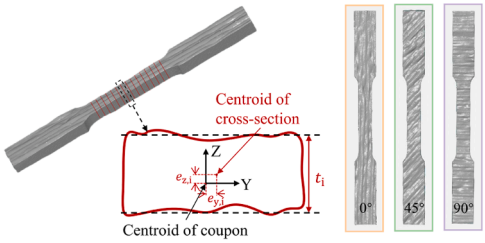

Fig. 8. The diagram of geometric measurements and coupons with different angles to print layer orientation.

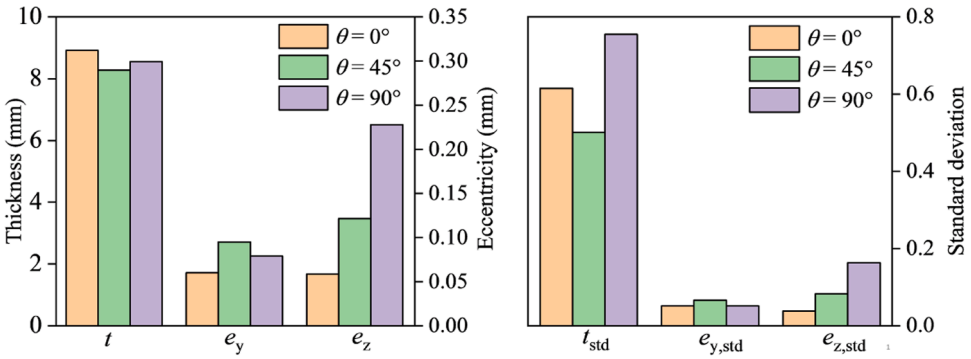

Fig. 9. The geometric properties of tensile coupon specimens.

the presence of surface irregularities in the WAAM specimens. The t_{std}, $e_{y,std}$, and $e_{z,std}$ values of the coupons with a θ of 0° were consistently smaller than those with a θ of 90°. This was attributed to the uniformity of cross-sections examined perpendicular to the direction of the deposition paths.

Fig. 10 shows the comparison of geometric properties between thin and thick tensile coupon specimens. The subscript 'k' and 'n' represent thick and thin specimens, respectively. For the tensile coupon specimens share the same printing orientation, the eccentricities on the Y-axis of thin specimens were consistently larger than those of thick specimens. Additionally, the normalized Y- and Z-eccentricities of thick specimens were consistently smaller than those of thin specimens. This indicates that the geometric properties of thick specimens were more uniform and stable. However, the surface roughness of WAAM plates, as indicated by the Y- and Z-eccentricities, has been proven independent of the plate thickness and is instead influenced by the process parameters [12,50].

4.1.2. Material properties

The stress-strain curves of all tensile coupons are shown in Fig. 11, including the full strain range on the left and a zoomed-in view limited to a strain of 1 % on the right. The axial strain field of the specimen at the peak of one stress-strain curve is also attached in Fig. 11, where the red region represents the maximum concentrated deformation. Material anisotropy was shown by the coupons from WAAM steel plates at angles of 0°, 45° and 90° to the print layer orientation. It showed that the yielding phases of the stress-strain curves were very prominent in the specimens with a θ of 0°, but gradually disappeared as the θ increased.

The average material properties, Young's modulus E, yield stress f_y (defined as the 0.2 % proof stress), ultimate tensile stress f_u, ultimate tensile strain ε_u, and fracture strain ε_f derived from stress-strain curves are presented in Table 5, which shows that the material properties generally decreased with the increase of θ.

The degree of anisotropy can be calculated using Eq. (7). As shown in Fig. 12, the stress and strain performance of the specimens were compared to show the degree of anisotropy. The anisotropic percentages

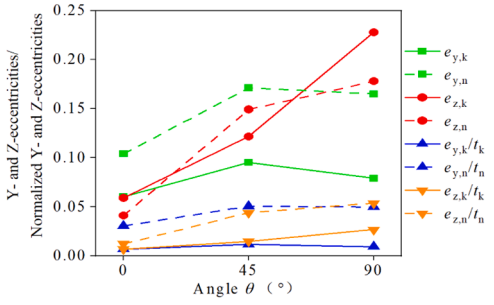

Fig. 10. Comparison of geometric properties between thin and thick tensile coupon specimens.

of yield stress and ultimate stress came to 7.4 %, and 7.8 % respectively, indicating a slight anisotropy. There was a larger difference of approximately 20 % between the ultimate tensile strain and fracture strain of the 0° and 90° specimens, showing a significant difference in the ductility and fracture performance of the material in different print layer orientations. The reason for the material anisotropy may be related to the initial defects caused by the surface undulation of the WAAM specimens.

$$p = \frac{|P_\theta - P_{\theta=0^\circ}|}{P_{\theta=0^\circ}} \times 100\%, \tag{7}$$

where p is the anisotropic degree; and P_θ represents the average properties of the specimens with an angle of θ.

Therefore, comprehensive research should be conducted to fully evaluate the performance of the WAAM steel material and consider the influence of anisotropy on its use in material design and practical application. In addition, the very limited difference in the material properties of specimens with θ of 0° and 45° was found and it was also the major reason for the print layer orientations selected for the single-shear bolted connection tests.

4.1.3. Elastic parameters

For four groups of coupons, the values of elastic parameters including Young's modulus E of coupons with θ of 0° (L), 45° (D) and 90° (T), and Poisson's ratios ν of coupons with θ of 0° (L) and 90° (T) were determined from the DIC system, according to the method proposed in the literature [10,51,52].

The values of Poisson's ratio were estimated as ratios between average transversal and longitudinal strains $\nu = \varepsilon_t/\varepsilon_l$ at selected cross sections of L and T coupons, as depicted in Fig. 13. In particular, in order to consider a possible uneven distribution of the transversal strains along the length of the coupon, the values of ε_t were taken as a mean over three measures taken at three different cross-sections.

Table 6 and Fig. 14 show the values of the elastic parameters for the L, D, and T coupons, compared with those of conventionally manufactured carbon steel (E = 210 GPa and ν = 0.3 according to EN 1993–1-1:2020 [45]). As shown in the previous Section 4.1.2, the mean values of Young's modulus along different print layer orientations show an anisotropic behaviour, lower than the reference (210 GPa). Moreover, Poisson's ratio values are larger than the reference (0.3), and also affected by the print layer orientations, with the ratio of L coupons ν_{TL} larger than those of T coupons ν_{LT}.

Fig. 15 compares the values of Young's modulus along one direction with the Poisson's ratio evaluated for the orthogonal direction, namely $E_L\nu_{LT}$ and $E_T\nu_{TL}$. The equation $E_L\nu_{LT} = E_T\nu_{TL}$ appears to reasonably match the data distribution pattern. However, further investigation is needed to confirm whether it exhibits orthotropic material behaviour.

Table 7 collects the values of the elastic parameters, including E_x, E_y, ν_{xy}, ν_{yx}, G_{xy}, of the orthotropic model for WAAM carbon steel calibrated from the experimental result. E_x and E_y are Young's moduli along the

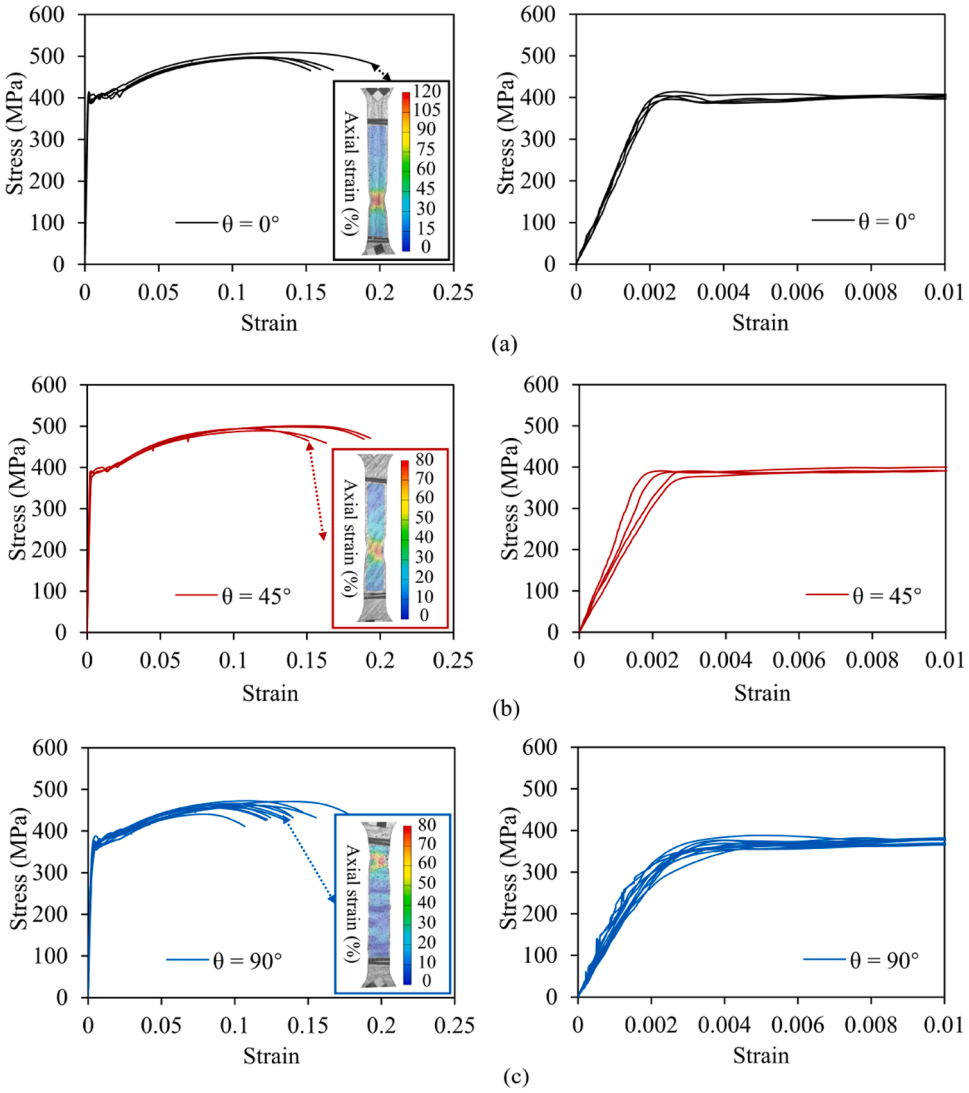

Fig. 11. The stress-strain whole curves (on the left) and zoom for strain lower than 1 % (on the right) for coupons with θ of (a) 0°, (b) 45°, and (c) 90°.

Table 5
Average material properties for coupons with a nominal thickness of 8 mm.

Nominal thickness (mm)	Actual thickness (mm)	θ (°)	E (GPa)	f_y (MPa)	f_u (MPa)	ε_u	ε_f
8	8.9	0	206	393	500	0.12	0.17
	8.3	45	196	386	496	0.13	0.17
	8.6	90	182	364	461	0.10	0.14

longitudinal and transverse direction to the print layer orientation, respectively; ν_{xy}, and ν_{yx} are the calibrated Poisson's ratios; and G_{xy} represents the shear modulus. These values can be expressed as follows according to the method proposed by Laghi et al. [52].

$$E_x = E_L; \quad E_y = E_T \tag{8a}$$

$$\nu_{xy} = \frac{E_x}{E_x + E_y} \times (\nu_{LT} + \nu_{TL}); \quad \nu_{yx} = \frac{E_y}{E_x + E_y} \times (\nu_{LT} + \nu_{TL}) \tag{8b}$$

$$G_{xy} = \left(\frac{4}{E_D} - \frac{1 - \nu_{xy}}{E_x} - \frac{1 - \nu_{yx}}{E_y}\right)^{-1} \tag{8c}$$

It is worth noting that the elastic parameters of WAAM carbon steel were evaluated from the results of the tensile tests on the as-built

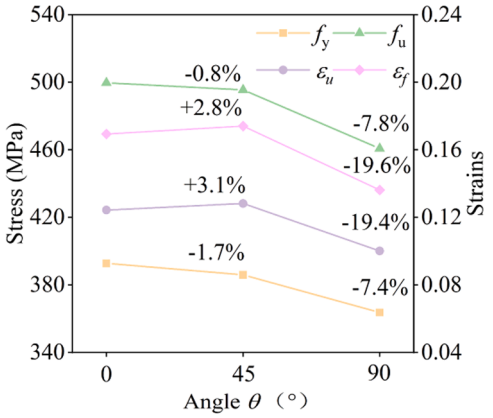

Fig. 12. The anisotropic analysis of the mechanical properties.

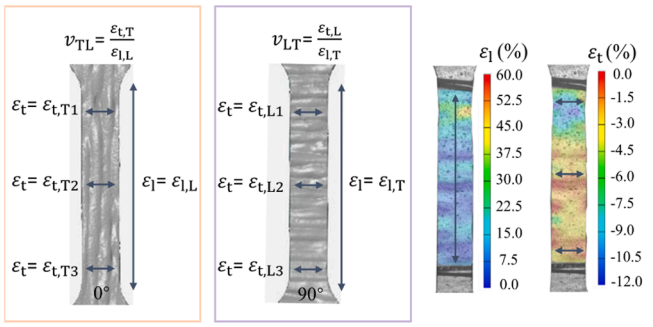

Fig. 13. Conceptual schematization of the estimation of the Poisson's ratio.

Table 6
WAAM elastic parameters from tensile tests.

	E (GPa)			*v*	
Group	L	D	T	LT	TL
1	190	198	161	0.35	0.45
2	211	237	204	0.43	0.49
3	217	157	199	0.42	0.42
4	205	194	167	0.40	0.50
Mean	206	196	183	0.40	0.47
COV	0.05	0.14	0.10	0.07	0.07

coupons. The surface undulations of the as-built coupons may cause fluctuations in the results.

4.2. Single-shear bolted connection tests

4.2.1. Test result summary

The detailed test results of all the single-shear bolted connection specimens using thick plates are given in Table 9. The ultimate capacity P_u was taken as the maximum load measured in tests, and U_{Pu} was the corresponding displacement at the maximum load. The variation range of ultimate capacity was within 97.1 kN to 268.8 kN, while the variation range of displacement was within 7.4 mm to 28.1 mm.

4.2.2. Failure mode and experiment phenomena

The typical specimens after failure are shown in Fig. 16, grouped with three different failure modes: net section tension, end-splitting, and tilt-bearing. All tested specimens exhibited fractures in the WAAM plates surrounding the bolt holes. The specimens that failed in net section tension were obviously characterized by relatively narrow plate widths. When the plate width was sufficiently large to prevent net section tension failure, the plate with a smaller end distance presented shear-out or end-splitting failure.

The typical shear-out failure was not discovered in the test, replaced

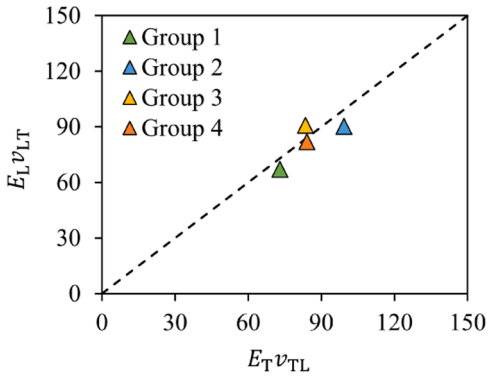

Fig. 15. Comparison of Young's moduli and Poisson's ratios along T and L directions.

Table 7
Elastic parameters of the orthotropic model for WAAM carbon steels.

Group	E_x (Gpa)	E_y (Gpa)	G_{xy} (Gpa)	v_{yx}	v_{xy}
1	190	161	75	0.44	0.37
2	211	204	86	0.46	0.45
3	217	199	50	0.44	0.40
4	205	167	68	0.50	0.41
Mean	206	183	70	0.46	0.41
COV	0.05	0.10	0.18	0.05	0.07

Note that the mean value of the shear modulus G_{xy} is 70 GPa, which is lower than the reference value of 81 GPa according to EN 1993-1-1 [45]. Table 8 highlights the discrepancies between experimental and calibrated Poisson's ratios. The values exhibit significant fluctuations, demonstrating poor consistency between experimental measurements and calibrated values, with a mean difference reaching ± 15 %. This discrepancy is notably larger than the ± 3 % reported by Laghi et al. for WAAM stainless steels [52], indicating that the orthotropic nature of WAAM carbon steel is not as pronounced.

Table 8
Discrepancy of experimental and calibrated Poisson's ratios.

Group	$(v_{yx}-v_{TL})/v_{TL}$ (%)	$(v_{xy}-v_{LT})/v_{LT}$ (%)
1	−18.16	23.24
2	−7.76	8.84
3	−4.19	4.19
4	−19.25	24.18
Mean	−12.34	15.11
COV	−0.53	0.58

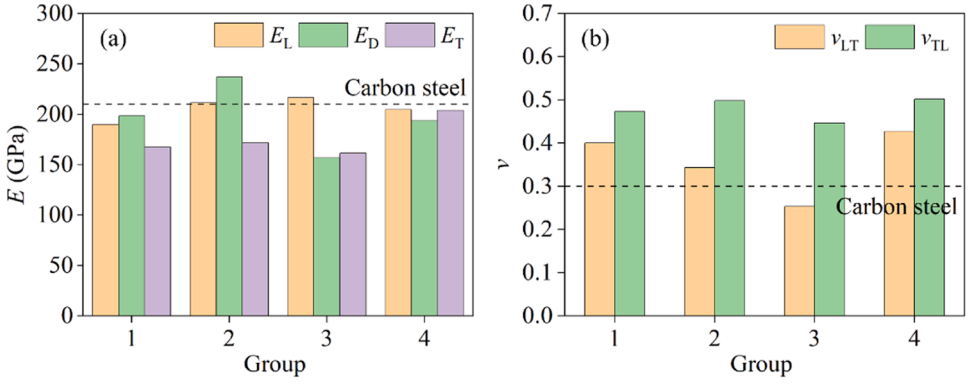

Fig. 14. Histograms of (a) Young's modulus and (b) Poisson's ratio values for WAAM stainless steels.

Table 9
Test results.

No.	Specimen	Failure mode	P_u (KN)	U_{Pu} (mm)	No.	Specimen	Failure mode	P_u (KN)	U_{Pu} (mm)
1	HS8−26−50−39	NS	97.1	9.3	14	VS8−26−50−39	NS	102.1	7.4
2	HS8−26−60−39	NS	145.3	12.6	15	VS8−26−60−39	NS	135.6	10.8
3	HS8−26−70−39	NS	162.1	16.3	16	VS8−26−70−39	NS	152.9	17.4
4	HS8−26−90−39	ES	169.0	19.1	17	VS8−26−90−39	TB	211.1	26.2
5	HS8−26−90−44	ES	170.8	18.1	18	VS8−26−90−44	TB	214.5	17.7
6	HS8−26−60−50	NS	137.4	9.4	19	VS8−26−60−50	NS	134.4	10.1
7	HS8−26−90−52	TB	216.1	20.6	20	VS8−26−90−52	TB	207.4	17.5
8	HS8−26−90−57	TB	189.6	13.3	21	VS8−26−90−57	TB	227.0	14.9
9	HS8−26−90−65	TB	195.9	13.4	22	VS8−26−90−65	TB	222.0	23.7
10	HS8−32−90−48[a]	ES	210.4	24.9	23	VS8−32−90−48[a]	TB	250.2	21.8
11	HS8−32−90−64[a]	NS	221.5	16.6	24	VS8−32−90−64[a]	TB	217.3	23.3
12	HS8−32−100−58[a]	TB	252.6	26.6	25	VS8−32−100−58[a]	TB	264.4	17.5
13	HS8−32−100−64[a]	TB	249.4	20.8	26	VS8−32−100−64[a]	TB	268.8	17.5
27	HS8−32−60−48	NS	124.7	8.4	30	HS8−32−70−45	NS	150.7	10.6
28	HS8−32−70−48	NS	162.8	10.4	31	VS8−26−90−32	TB	182.0	28.1
29	HS8−32−90−42	ES	161.5	14.6	32	VS8−32−90−39	ES	161.6	18.2

Note: NS = net section tension failure; ES = end-splitting failure; TB = tilt-bearing failure.
[a] Specimens were tested to failure using a 1000 kN Instron 8805 testing machine.

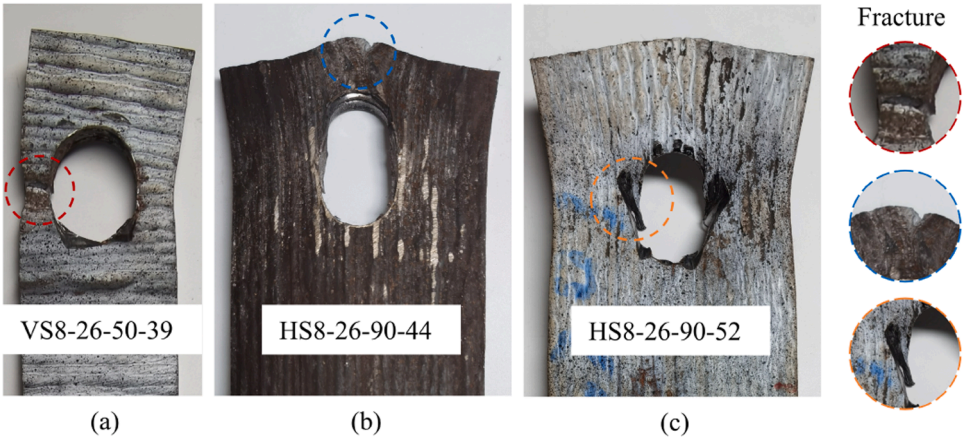

Fig. 16. Typical failure modes: (a) net section tension, (b) end-splitting, and (c) tilt-bearing failure.

by the end-splitting failure. The fracture was generated from the plate end and gradually spread towards the bolt hole. When the plate featured a larger end distance, it tended to curl, and the bolt punched through, causing fractures around the bolt hole that ultimately resulted in a tilt-bearing failure. For the single-shear bolted connection, it is generally assumed that thick plates exhibit less susceptibility to tilting in comparison to thin plates [42]. However, in our tests, the tested thick plates which failed in tilt-bearing were observed to experience varying degrees of tilting.

Fig. 17 shows the typical load-displacement curves of specimens with the three failure modes. As shown in Fig. 17(a), the load-displacement curves of specimens with different widths that failed in net section tension displayed an increase in ultimate capacities with increasing widths. In addition, the stiffnesses of the specimens, which were reflected by the slopes of the load-displacement curves, also increased with increasing widths. The axial strain ε_{yy} fields at different displacements obtained by the DIC system for specimen VS8–26-60–50 are displayed in Fig. 18. It can be observed that the deformation was mainly concentrated in the net section on the right side. As the displacement increased, the specimen underwent necking across the width and thickness of the plates until fracture.

The load-displacement curves of all the five specimens that failed in end-splitting are illustrated in Fig. 17(b). For specimen HS8–26-90–44, the transverse strain ε_{xx} fields visualised by the DIC system are displayed in Fig. 19. As the bolt compressed, the material in front of it was squeezed out and a significant rotation at the net cross-section was observed. This resulted in the development of high transverse tensile stresses along the width direction until a fracture originated from the plate end.

Fig. 17(c) shows the typical load-displacement curves of the bolted connections corresponding to tilt-bearing failure mode. For specimen HS-22–60-40, the axial strain ε_{yy} fields at different displacements obtained by the DIC system are displayed in Fig. 20. The compressive strain on the downstream of the bolt hole and the tensile strain on the side of the bolt hole gradually increased as the stress increased. Corresponding to the rapid intensification of plate curling, a decrease in the load-displacement curve was observed.

4.2.3. *Analysis of anisotropy behaviours*

For the 13 pairs of specimens with similar geometric parameters but different print layer orientations, anisotropic behaviours were observed. Among them, four pairs of specimens exhibited different failure modes, as shown in Fig. 21. The locations of the fractures were marked with red lines. From visual observation of the failure phenomenon, both HS8–32-90–64 and VS8–32-90–48 exhibited a combined failure of net section tension and tilt-bearing. However, upon further analysis of their ultimate capacity and fracture development status, it was determined that the two specimens failed due to net section tension and tilt-bearing, respectively.

The divergence in general trends was the propensity of HS specimens to fail in end-splitting, whereas VS specimens tended to fail in tilt-bearing. VS specimens had higher transverse resistance due to their

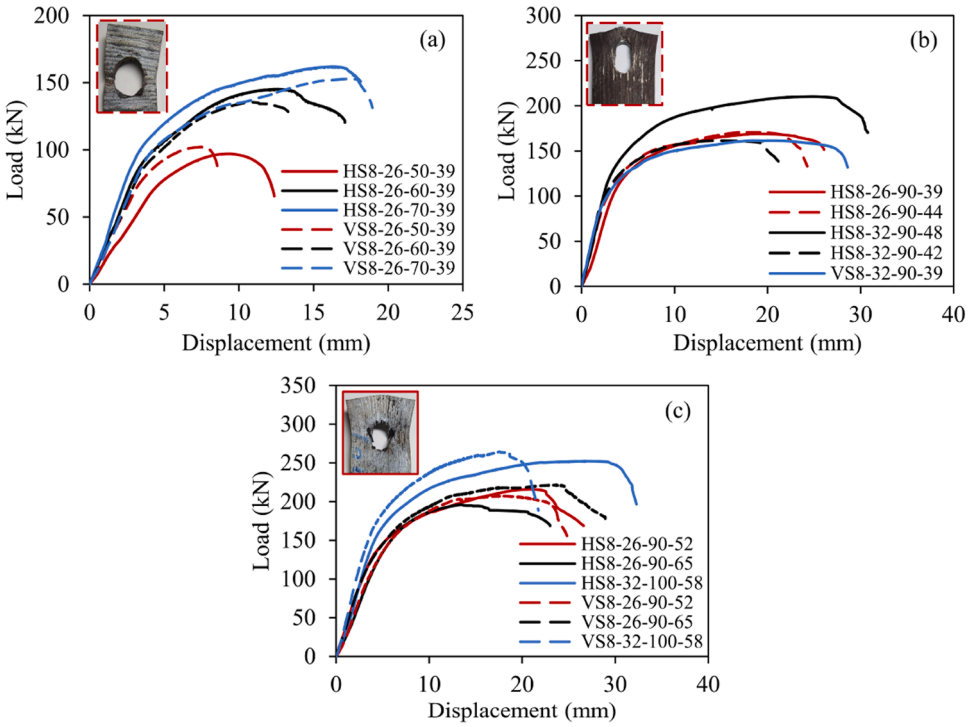

Fig. 17. Typical load-displacement curves of specimens with different failure modes: (a) net section tension, (b) end-splitting and (c) tilt-bearing failure.

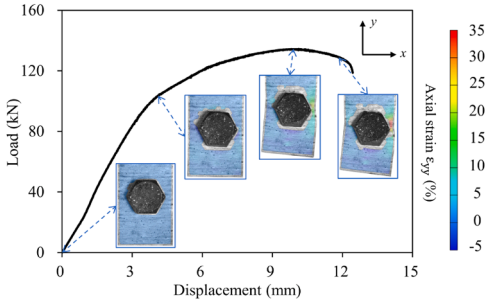

Fig. 18. Strain fields at different displacements for specimen VS8–26-60–50.

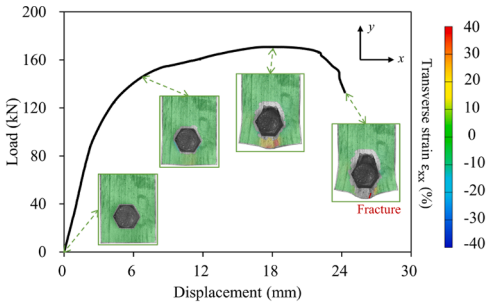

Fig. 19. Strain fields at different displacements for specimen HS8–26-90–44.

print layers being parallel to the stress direction, resulting in the material in front of the bolt hole curling under the compression of the bolt. Contrarily, fractures in HS specimens developed from the plate end due to their relatively weaker transverse resistance. Owing to a deviation in the position of the bolt hole in HS8–32-90–64, the net section on its right side was reduced, resulting in a net section tension failure.

The normalised ultimate capacities ratios $P_{u,90^\circ}/tf_{u,eff,90^\circ}$ and $P_{u,0^\circ}/tf_{u,eff,0^\circ}$ of the VS and HS specimens are compared in Fig. 22. The mean

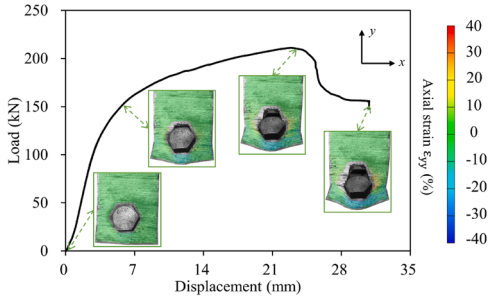

Fig. 20. Strain fields at different displacements for specimen VS8–26-90–39.

of normalised ultimate capacities ratios reached 1.11, exceeding the anisotropic degree of WAAM material in terms of ultimate stress. For specimens exhibiting net section tension failure, the difference in ultimate capacity between VS and HS specimens remained within 10 %. This difference was more pronounced for specimens exhibiting tilt-bearing failure, with the ratio of $P_{u,90^\circ}/tf_{u,eff,90^\circ}$ and $P_{u,0^\circ}/tf_{u,eff,0^\circ}$ displaying an overall trend greater than unity. In addition, an examination of pairs of specimens exhibiting inconsistent failure modes revealed that the normalized ultimate capacities of VS specimens with tilt-bearing failure were higher. However, the differences in displacements did not show any potential trends. Overall, the specimens with similar geometric parameters but different print layer orientations exhibited slight anisotropy in terms of failure modes and ultimate capacities.

4.2.4. *Analysis of the thickness influence*

Our previous experiments focused on the WAAM steel bolted connections composed of thin plates (nominal thickness = 3 mm) [35]. For bolted connections composed of thick and thin plates whose plate dimensions had the same e_1/d and e_2/d, it was found that the ultimate capacities of bolted connection specimens were influenced by plate thickness. The normalised ultimate capacities P_u/Af_u of WAAM steel bolted connections composed of thick and thin plates (nominal thickness = 3 mm) are compared in Fig. 23.

Fig. 21. Four pairs of specimens with different failure modes.

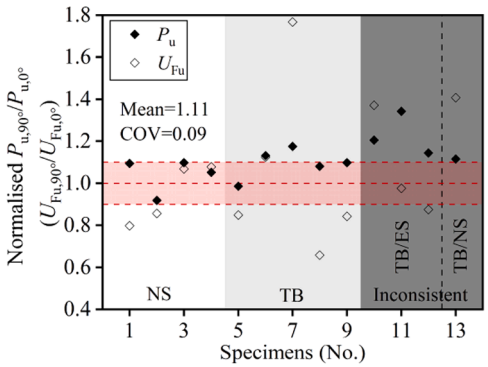

Fig. 22. Comparison of ultimate capacities and displacements on different print layer orientations.

The normalised ultimate capacities P_u/Af_u of bolted connections composed of thick plates were usually higher than those of thin plates under different e_1/d and e_2/d. Although in some cases, such as $e_2/d = 1.2$, the normalised ultimate capacities of thin plates were higher, the difference was slight. It indicates that the bolted connections composed of thick plates can better utilize the cross-sectional strength of the material and provide more reliable performance. However, the bolt connections with $e_1/d = 1.4$ showed significant and unusual difference. The reason may be that the bolted connections with thick plates mainly exhibited end-splitting failure, while the bolted connections with thin plates mainly exhibited net section tension failure. By comparison, the response of specimens failing in net section tension failure was more stable.

5. Comparison of design predictions

5.1. General

In this section, the failure modes and ultimate loads of the tested specimens were compared against predictions of the design equations previously summarized in Section 2, to evaluate the suitability of available design methods for WAAM steel bolted connections. The comparisons of tested ultimate loads and predicted ultimate capacities are summarized in Fig. 24.

For application to all specimens, AISC 360 [44] demonstrated a best average test-to-predicted capacity ratio of 1.00 but an unsatisfactory

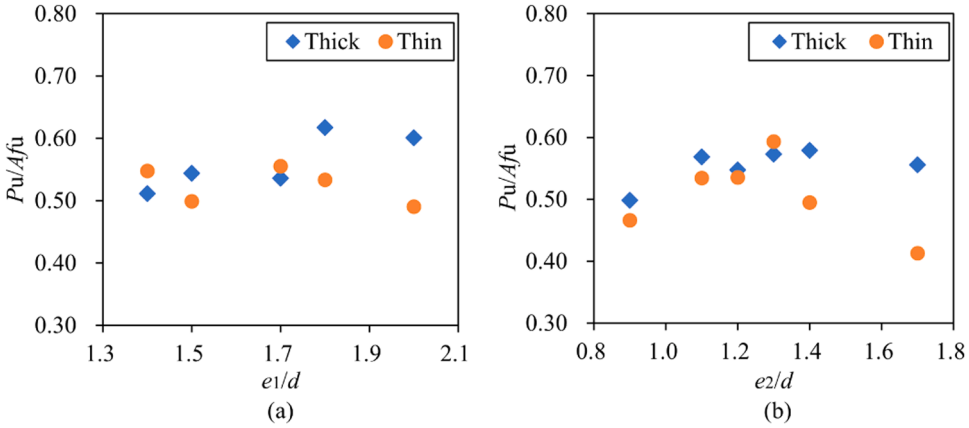

Fig. 23. Comparison of ultimate capacities and displacements on different print layer orientations.

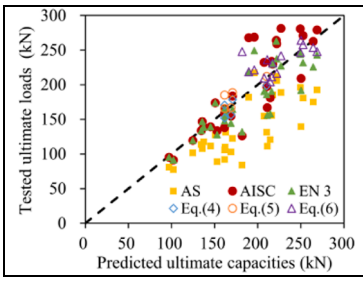

Summary of test-to-predicted ratio		
Design codes	Mean	COV
AS 4100	1.39	0.20
AISC 360	1.00	0.15
Eurocode 3	1.06	0.14
Eq. (4)	1.02	0.06
Eq. (5)	0.95	0.06
Eq. (6)	0.96	0.09

Fig. 24. Comparison of tested ultimate loads and predicted ultimate capacities.

coefficient of variation (COV) of 0.15. The results were also reflected in the left scatter plot. Except for a few red dots that fell on the diagonal with $k = 1$, other red dots were evenly distributed in the upper and lower parts of the diagonal, resulting in an average ratio close to 1.00 and a large COV. It reflected the predictive instability of AISC 360 [44]. A similar prediction performance occurred in Eurocode [45,46], but it showed an underestimation of 6 % of the tested ultimate loads. Although the design equations of AS 4100 [43] and Eurocode [45,46] obtained an overall average conservatism, AS 4100 [43] was more conservative than Eurocode [45,46], also with more instability. It can be clearly observed that almost all the yellow squares (AS 4100 [43]) were distributed in the lower half of Fig. 24, indicating an overall underestimation.

Compared with the three specifications, the prediction results of Eq. (4) [33] and Eq. (5) [34] specific to shear-out failure and Eq. (6) [36] specific to tilt-bearing failure were usually both accurate and stable. One possible factor contributing to this phenomenon may be that the three specifications misjudged the failure modes during prediction, resulting in unsatisfactory results. It will be discussed in detail below for each failure mode.

5.2. Net section tension failure

The test-to-predicted capacity ratios of individual specimens failing by net section tension are summarized in Table 10. Occasionally, the specimens were incorrectly predicted as a shear-out failure, resulting in low accuracy in predicting failure modes. The failure mode prediction accuracy of AS 4100 [43] did not even exceed 0.5, corresponding with a lower average test-to-predicted capacity ratio of 1.28.

AISC 360 [44] and Eurocode [45] shared the same equation for net section tension failure with the same correction factors of 1. They agreed with the test data with reasonable accuracy, reaching an average ratio of less than 1.01 and a COV of less than 0.09. Some specimens, such as HS8–26-70–39 and VS8–26-70–39, were mistakenly identified as shear-out failure, and the different design codes for shear-out failure between the two specifications resulted in slight differences of prediction. Considering these results, for WAAM steel bolted connections composed of thick plates failing in net section tension, the correction factor meant for reduction is unnecessary.

Table 10
Assessments of design codes for net section tension failure.

Specimen	AS 4100		AISC 360		Eurocode 3	
	FM	P_u/P_{AS}	FM	P_u/P_{AISC}	FM	P_u/P_{EN3}
HS8−26−50−39	NS	1.20	NS	1.02	NS	1.02
HS8−26−60−39	(SO)	1.31	NS	1.04	NS	1.04
HS8−26−70−39	(SO)	1.47	(SO)	0.98	(SO)	1.05
HS8−26−60−50	NS	1.17	NS	0.99	NS	0.99
HS8−32−60−48	NS	1.23	NS	1.04	NS	1.04
HS8−32−70−48	(SO)	1.24	NS	1.02	NS	1.02
HS8−32−90−64	(SO)	1.04	NS	0.84	(SO)	0.84
HS8−32−70−45	(SO)	1.18	NS	0.87	NS	0.87
VS8−26−50−39	NS	1.32	NS	1.12	NS	1.12
VS8−26−60−39	(SO)	1.26	NS	0.92	NS	0.92
VS8−26−70−39	(SO)	1.72	(SO)	1.14	(SO)	1.20
VS8−26−60−50	NS	1.18	NS	1.00	NS	1.00
FMPA	0.42		0.83		0.75	
Mean		1.28		1.00		1.01
COV		0.13		0.09		0.09

Note: FMPA =failure mode prediction accuracy; failure mode in brackets means it was different from the test result.

5.3. End-splitting failure

The lack of a specific design equation for end-splitting failure could be attributed to the fact that current specifications did not clearly distinguish between shear-out and end-splitting failure. Therefore, due to the similar mechanical behaviours between the two failure modes, the ultimate capacities of specimens failing by end-splitting were predicted using the equations for shear-out failure in many studies [53,54].

In Table 11, the assessments of design equations for end-splitting failure using shear-out equations are presented. It is evident that except for AS 4100 [43], other design equations exhibited satisfying predictive performance. Eq. (4) [33] proposed a new active shear plane, which had the highest accuracy with an underestimation of 2 % and a COV of 0.06. Eq. (5) [34] added a factor account for the contribution of the catenary action on the basis of Eq. (4) [33], but it led to a 5 % slight overestimation. On the contrary, AISC 360 [44] led to a 5 % underestimation.

Overall, the COVs of these five design codes were relatively small, which were less than 0.08, indicating their stable prediction performance. It was mainly because the failure modes were correctly predicted to be shear-out failure.

5.4. Tilt-bearing failure

The failure mode of tilt-bearing has not been integrated into current design standards. As a result, it is typically predicted as a net section tension or shear-out failure, with the corresponding ultimate capacity being derived accordingly, as shown in Table 12. AS 4100 [43] caused a significant underestimation reaching 1.42, due to the conservatism of the shear-out design provisions. Although AISC 360 [44] and Eurocode equations [46] provided a relatively satisfactory test-to-predict ratio, their COVs were rather larger. This could be attributed to a significant difference between the design codes used and the mechanical mechanism of tilt-bearing failure.

After discovering that the plate width, plate thickness, and bolt diameter had meaningful influences on the ultimate capacities of tilt-bearing specimens, Eq. (6) [36] was proposed for tilt-bearing failure in thin plates ($t \leq 3$ mm). The ultimate capacities were accurately predicted by Eq. (6) [36], with an overestimation within 4 % and an appropriate COV of 0.09. It indicated that the design equation was also suitable for WAAM steel bolted connections composed of thick plates.

5.5. Comparison with bolted connections composed of thin plates

Our previous experiments have compared the design prediction of WAAM steel bolted connections composed of thin plates with experimental results [36]. It was found that existing design provision for conventionally manufactured steel had certain applicability for WAAM steel bolted connections. Fig. 25 compared the prediction performance comparison of WAAM bolted connections composed of thin and thick plates. In terms of average test-to-predict ratio of each design provision, the overall values of bolted connection composed of thick plates were smaller than those of thin plates, which were closer to the experimental ultimate loads. The difference was that Eq. (5) [34] and Eq. (6) [36] overestimated the ultimate capacity of bolted connection composed of thick plates but underestimated the ultimate capacity of bolted connection composed of thin plates. In addition, the COVs of thick plates were smaller than these of thin plates.

Table 11
Assessments of design codes for end-splitting failure using shear-out equations.

Specimen	AS 4100		AISC 360		Eurocode 3		Eq. (4)	Eq. (5)
	FM	P_u/P_{AS}	FM	P_u/P_{AISC}	FM	P_u/P_{EN3}	$P_u/P_{Eq.(4)}$	$P_u/P_{Eq.(5)}$
HS8-26-90-39	SO	1.64	SO	1.09	SO	1.17	1.08	1.01
HS8-26-90-44	SO	1.39	SO	0.93	SO	1.04	0.96	0.91
HS8-32-90-48	SO	1.60	SO	1.07	SO	1.13	1.06	0.99
HS8-32-90-42	SO	1.53	SO	1.02	SO	0.98	0.95	0.87
VS8-32-90-39	SO	1.75	SO	1.17	SO	1.09	1.06	0.97
Mean		1.58		1.05		1.08	1.02	0.95
COV		0.08		0.08		0.06	0.06	0.06

Table 12
Assessments of design codes for tilt-bearing failure.

Specimen	AS4100		AISC 360		Eurocode 3		Eq. (6)
	P_u/P_{AS}		P_u/P_{AISC}		P_u/P_{EN3}		$P_u/P_{Eq.(6)}$
HS8−26−90−52	SO	1.39	SO	0.92	SO	1.14	1.02
HS8−26−90−57	SO	1.04	NS	0.71	SO	0.87	0.87
HS8−26−90−65	SO	0.90	NS	0.73	SO	0.79	0.89
HS8−32−100−58	SO	1.40	SO	0.93	SO	1.09	0.98
HS8−32−100−64	SO	1.27	NS	0.89	SO	1.02	1.01
VS8−26−90−39	SO	1.90	SO	1.26	SO	1.35	0.89
VS8−26−90−44	SO	1.78	SO	1.18	SO	1.36	1.05
VS8−26−90−52	SO	1.34	SO	0.89	SO	1.09	0.99
VS8−26−90−57	SO	1.20	NS	0.81	SO	1.00	0.94
VS8−26−90−65	SO	1.08	NS	0.86	SO	0.94	1.03
VS8−32−90−48	SO	1.79	SO	1.20	SO	1.31	0.95
VS8−32−90−64	SO	1.17	NS	0.95	NS	0.95	0.94
VS8−32−100−58	SO	1.51	SO	1.01	SO	1.17	1.04
VS8−32−100−64	SO	1.40	NS	0.96	SO	1.11	1.09
VS8−2−90−32	SO	2.16	SO	1.44	SO	1.38	0.73
Mean		1.42		0.98		1.10	0.96
COV		0.24		0.20		0.16	0.09

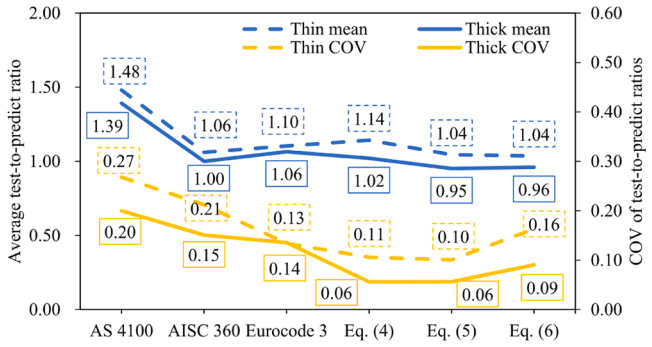

Fig. 25. Prediction performance comparison of bolted connections composed of thin and thick plates.

Overall, it could be assumed that thickness of connected plates of WAAM bolted connections had a certain influence on the prediction results, and various design provisions performed more accurately and stably on bolted connections composed of thick plates.

6. Conclusions

The material properties of WAAM steels and the structural behaviours of WAAM steel bolted connections have been investigated in this paper. The fundamental material properties of WAAM steels exhibited slight anisotropy in stress and significant differences in ductility and fracture performance. For this reason, bolted connection specimens with different print layer orientations were studied, and anisotropy behaviours in terms of failure modes and ultimate capacities were also observed. Based on the results, the following conclusions were drawn:

1) The yield stress and ultimate stress difference came to 7.4 %, and 7.8 % respectively, indicating a slight anisotropy, while the mean of normalised ultimate capacities difference of WAAM steel bolted connections reached 11 %, which was higher than that of WAAM material.

2) The existing design provisions for conventionally manufactured steel bolted connections were used to evaluate the ultimate capacities of WAAM single-shear bolted connection specimens. For different failure modes, the best predictions for net section tension, end-splitting, and tilt-bearing failure were obtained by AISC 360 [44], Eq. (4) [33], and Eq. (6) [36], respectively. The analysis showed that the design provisions were suitable for WAAM bolted connections.

3) Compared with WAAM steel bolted connection composed of thin plates, thick plates had more stable response during tests and better applicability to existing design provisions.

4) Despite their usefulness, existing design codes have limitations on the identification of failure modes and a distinct specification for WAAM steel should be developed. Additional research is required to promote the implementation of 3D printing technology in real-world engineering projects.

CRediT authorship contribution statement

Weijian Zhao: Writing – review & editing, Supervision, Conceptualization. **Yunyi Liu:** Writing – original draft, Validation, Methodology, Investigation, Formal analysis, Data curation. **Jun Ye:** Writing – review & editing, Supervision, Resources, Project administration, Methodology, Funding acquisition, Conceptualization. **Zhen Wang:** Writing – review & editing, Supervision, Methodology, Investigation. **Yang Zhao:** Writing – review & editing, Methodology, Investigation, Funding acquisition, Conceptualization. **Hongjia Lu:** Writing – review & editing, Supervision, Methodology, Investigation. **Guan Quan:** Writing – review & editing, Supervision, Methodology, Investigation, Conceptualization.

Declaration of Competing Interest

The authors declare that they have no known competing financial interests or personal relationships that could have appeared to influence the work reported in this paper.

Acknowledgements

The authors would like to acknowledge the financial support to this project by the National Natural Science Foundation of China (No. 52078452, 52208215), the Basic Public Research Project of Zhejiang Province (No. LGG22E080005, LQ22E080008) and the Australian Research Council (No. FL190100014).

Data availability

The data presented in this work will be made available upon reasonable request.

References

[1] Gardner L. Metal additive manufacturing in structural engineering – review, advances, opportunities and outlook. Structures 2023;47:2178–93.
[2] Hadjipantelis N, Shah IH, Walter L, Myers RJ, Gardner L. Metal additively versus conventionally manufactured structures – an environmental life cycle assessment. ce/Pap 2023;6:672–7.
[3] Kanyilmaz A, Demir AG, Chierici M, Berto F, Gardner L, Kandukuri SY, et al. Role of metal 3D printing to increase quality and resource-efficiency in the construction sector. Addit Manuf 2022;50:102541.
[4] Laghi V, Gasparini G. Explorations of efficient design solutions for wire-and-arc additive manufacturing in construction. Structures 2023;56:104883.
[5] Lange J, Feucht T, Erven M. 3D-printing with steel - additive manufacturing connections and structures. ce/Pap 2021;4:2–7.
[6] Ye J, Kyvelou P, Gilardi F, Lu H, Gilbert M, Gardner L. An end-to-end framework for the additive manufacture of optimized tubular structures. IEEE Access 2021;9:165476–89.
[7] Feucht T, Waldschmitt B, Lange J, Erven M. Additive manufacturing of a bridge in situ. Steel Constr 2022;15:100–10.
[8] Gardner L, Kyvelou P, Herbert G, Buchanan C. Testing and initial verification of the world's first metal 3D printed bridge. J Constr Steel Res 2020;172:106233.
[9] Huang C, Kyvelou P, Zhang R, Ben Britton T, Gardner L. Mechanical testing and microstructural analysis of wire arc additively manufactured steels. Mater Des 2022;216:110544.
[10] Hadjipantelis N, Weber B, Buchanan C, Gardner L. Description of anisotropic material response of wire and arc additively manufactured thin-walled stainless steel elements. Thin Walled Struct 2022;171:108634.
[11] Kyvelou P, Slack H, Buchanan C, Wadee MA, Gardner L. Material testing and analysis of WAAM stainless steel 2021;4:1702–9.
[12] Laghi V, Palermo M, Gasparini G, Girelli VA, Trombetti T. On the influence of the geometrical irregularities in the mechanical response of wire-and-arc additively manufactured planar elements. J Constr Steel Res 2021;178:106490.
[13] Laghi V, Arrè L, Tonelli L, Di Egidio G, Ceschini L, Monzón I, et al. Mechanical and microstructural features of wire-and-arc additively manufactured carbon steel thick plates. Int J Adv Manuf Technol 2023;127:1391–405.
[14] Huang C, Li L, Pichler N, Ghafoori E, Susmel L, Gardner L. Fatigue testing and analysis of steel plates manufactured by wire-arc directed energy deposition. Addit Manuf 2023;73:103696.
[15] Chen M-T, Zhang T, Gong Z, Zuo W, Wang Z, Zong L, et al. Mechanical properties and microstructure characteristics of wire arc additively manufactured high-strength steels. Eng Struct 2024;300.
[16] Huang C, Kyvelou P, Gardner L. Stress-strain curves for wire arc additively manufactured steels. Eng Struct 2023;279:115628.
[17] Laghi V, Palermo M, Gasparini G, Girelli VA, Trombetti T. Experimental results for structural design of wire-and-arc additive manufactured stainless steel members. J Constr Steel Res 2020;167:105858.
[18] Kyvelou P, Huang C, Gardner L, Buchanan C. Structural testing and design of wire arc additively manufactured square hollow sections. J Struct Eng 2021;147:04021218.
[19] Huang C, Meng X, Buchanan C, Gardner L. Flexural buckling of wire arc additively manufactured tubular columns. J Struct Eng 2022;148:04022139.
[20] Huang C, Meng X, Gardner L. Cross-sectional behaviour of wire arc additively manufactured tubular beams. Eng Struct 2022;272:114922.
[21] Guo X, Kyvelou P, Ye J, Gardner L. Experimental investigation of wire arc additively manufactured steel T-stub connections. J Constr Steel Res 2023;211:108106.
[22] Erven M, Lange J, Feucht T. 3D-printing with steel of a bolted connection. ce/Pap 2021;4:825–32.
[23] Evans S, Wang J, Pan J, Xu F. Experimental study of wire arc additively manufactured steel sections stiffened by sinusoidal waves. Structures 2024;65.
[24] Evans SI, Xu F, Wang J. Experiments on the material and stability performance of slender WAAM plated structures. Thin Walled Struct 2024;202.
[25] Huang C, Zheng Y, Chen T, Ghafoori E, Gardner L. Fatigue crack growth behaviour of wire arc additively manufactured steels. Int J Fatigue 2023;173:107705.
[26] Evans S, Hadjipantelis N, Wang J. Effects of deposition rate on local stability of wire arc additively manufactured outstand elements. ce/Pap 2023;6:678–83.
[27] Grebner P, Lange J. 3D-printing with steel on thin sheets for application in free form façade construction: welding process development and material properties. ce/Pap 2023;6:666–71.
[28] Laghi V, Palermo M, Bruggi M, Gasparini G, Trombetti T. Blended structural optimization for wire-and-arc additively manufactured beams. Prog Addit Manuf 2022;8:381–92.
[29] Laghi V, Babovic N, Benvenuti E, Kloft H. Blended structural optimization of steel joints for wire-and-arc additive manufacturing. Eng Struct 2024;300:117141.
[30] Teh LH, Gilbert BP. Net section tension capacity of bolted connections in cold-reduced steel sheets. J Struct Eng 2012;138:337–44.
[31] Salih EL, Gardner L, Nethercot DA. Numerical investigation of net section failure in stainless steel bolted connections. J Constr Steel Res 2010;66:1455–66.
[32] Teh LH, Clements DDA. Block shear capacity of bolted connections in cold-reduced steel sheets. J Struct Eng 2012;138:459–67.
[33] Teh LH, Uz ME. Ultimate shear-out capacities of structural-steel bolted connections. J Struct Eng 2015;141:04014152.
[34] Xing H, Teh LH, Jiang Z, Ahmed A. Shear-out capacity of bolted connections in cold-reduced steel sheets. J Struct Eng 2020;146:04020018.
[35] Clements DDA, Teh LH. Active shear planes of bolted connections failing in block shear. J Struct Eng 2013;139:320–7.
[36] Teh Lip H, Uz Mehmet E. Ultimate tilt-bearing capacity of bolted connections in cold-reduced steel sheets. J Struct Eng 2017;143:04016206.
[37] Ding C, Torabian S, Schafer BW. Strength of bolted lap joints in steel sheets with small end distance. J Struct Eng 2020;146:04020270.
[38] Kamtekar AG. On the bearing strength of bolts in clearance holes. J Constr Steel Res 2012;79:48–55.
[39] Teh LH, Uz ME. Combined bearing and shear-out capacity of structural steel bolted connections. J Struct Eng 2016;142:04016098.
[40] Elliott MD, Teh LH, Ahmed A. Behaviour and strength of bolted connections failing in shear. J Constr Steel Res 2019;153:320–9.
[41] Może P. Bearing strength at bolt holes in connections with large end distance and bolt pitch. J Constr Steel Res 2018;147:132–44.
[42] Salih EL, Gardner L, Nethercot DA. Bearing failure in stainless steel bolted connections. Eng Struct 2011;33:549–62.
[43] AS 4100. Steel structures. Standards Association of Australia. Australia. 2020.
[44] AISC 360. Specification for structural steel buildings. American Institute of Steel Construction. Chicago. 2022.
[45] Eurocode 3 - design of steel structures – part 1–1: general rules and rules for builidng. European Committee for Standardisation. Brussels. 2020.
[46] Eurocode 3 - design of steel structures – part 1–8: joints. European Committee for Standardisation. Brussels. 2024.
[47] AS/NZS 4600. Cold-formed steel structures. Australian/New Zealand Standard. Sydney. 2018.
[48] Liu Y, Ye J, Yang Y, Quan G, Wang Z, Zhao W, et al. Experimental study on wire and arc additively manufactured steel double-shear bolted connections. J Build Eng 2023;76:107330.
[49] Ye J, Liu Y, Yang Y, Wang Z, Zhao O, Zhao Y. Testing, analysis and design of wire and arc additively manufactured steel bolted connections. Eng Struct 2023;296.
[50] Laghi V, Palermo M, Gasparini G, Veljkovic M, Trombetti T. Assessment of design mechanical parameters and partial safety factors for wire-and-arc additive manufactured stainless steel. Eng Struct 2020;225:111314.
[51] Kyvelou P, Slack H, Daskalaki Mountanou D, Wadee MA, Britton TB, Buchanan C, et al. Mechanical and microstructural testing of wire and arc additively manufactured sheet material. Mater Des 2020;192:108675.
[52] Laghi V, Tonelli L, Palermo M, Bruggi M, Sola R, Ceschini L, et al. Experimentally-validated orthotropic elastic model for wire-and-arc additively manufactured stainless steel. Addit Manuf 2021;42:101999.
[53] Guo X, Kyvelou P, Ye J, Teh LH, Gardner L. Experimental investigation of wire arc additively manufactured steel single-lap shear bolted connections. Thin Walled Struct 2022;181:110029.
[54] Guo X, Kyvelou P, Ye J, Teh LH, Gardner L. Experimental study of DED-arc additively manufactured steel double-lap shear bolted connections. Eng Struct 2023;281:115736.